FFEMS Fatigue & Fracture of Engineering Materials & Structures
ORIGINAL CONTRIBUTION
doi: 10.1111/ffe.12266

Study of the fracture of ferritic ductile cast iron under different loading conditions

D. O. FERNANDINO and R. BOERI

Metallurgy Division, INTEMA – National University of Mar del Plata – CONICET, Mar del Plata, B7608FDQ, Argentina

Received Date: 20 August 2014; Accepted Date: 2 November 2014; Published Online: 8 December 2014

ABSTRACT This work is a continuation of the studies presented in a recent paper by the authors, where the fracture surfaces of pearlitic ductile cast iron under different loading conditions were exhaustively analysed. In this study, fracture surfaces of ferritic ductile cast iron (or ferritic spheroidal graphite cast iron) generated under impact, bending and fatigue loading conditions were characterised and compared. The fracture surfaces were characterised qualitatively and quantitatively from the observation under a scanning electron microscope. The fracture mechanisms in each case were identified. For impact tests, as test temperature increases, the dominant fracture mechanism changes from brittle to ductile. For bending tests, a fully ductile fracture micromechanism dominates the surface. In fatigue tests, the surface shows a mix of flat facets that appear to be cleavage facets and ductile striations, but the typical fatigue striations are not easily found on the fracture surface. Methodologies for the determination of the macroscopic direction of main crack propagation in both ductile and brittle failure modes are proposed. These allow identifying main crack propagation direction with good approximation.
The results are potentially useful to identify the nature of loading conditions in a fractured specimen of ferritic spheroidal graphite cast iron. The authors believe that it is necessary to extend the methodologies proposed in samples with different geometry and size, before they can be used to provide additional information to the classical fractographic analysis.

Keywords bending; ductile iron; impact; fatigue; fractography; fracture surface.

NOMENCLATURE

M = Mean value of the set of data
Me = Median value of the set of data
Mo = Mode value of the set of data
Y = Length of the nodular contour in parallel axis to the main crack propagation direction
X = Length of the nodular contour in perpendicular axis to the main crack propagation direction
α = Angle between the major axis of the equivalent ellipse and the main crack propagation direction

INTRODUCTION

Ferritic ductile iron (FDI) is a type of ductile cast iron (DI) usually used in marine applications, valves, fittings, truck and agricultural implements, automotive steering knuckles and other applications where ductility and good impact properties are required. It can be used to replace low-carbon steel.[1] As DI parts are extensively applied, failure events may take place, and it is essential to perform failure analyses to identify the causes of the fracture and to provide corrective actions to guarantee safe operation. It is generally accepted that after the fracture of a metallic material, some characteristic features of the fracture surface can be used to identify the dominant fracture mechanism during failure.[2,3] For example, it has been established that the four common fracture mechanisms involved in metal fracture are ductile fracture, cleavage fracture, intergranular fracture and fatigue.[4–6] However, when the material is FDI, there is a noticeable lack of detailed information about the relationship between fracture surface features, load conditions and the dominant fracture mechanism. The main effect of changes in the

Correspondence: D. O. Fernandino. E-mail: dfernandino@fi.mdp.edu.ar

fracture surfaces caused by impact or bending loads, fatigue, exposure to low temperature or environmental embrittlement is just described qualitatively, but information that can lead to the identification of the root causes of fracture from a fractographic analysis is scarce. In addition, there are no methods that can be used to identify the direction of crack propagation in the fracture surface of a particular FDI. In general, the investigations about DI have been focused on the study of the mechanical properties using mechanical tests under different loading configurations.[7–14] Some articles analyse the effect of the graphite nodule on the fracture process either experimentally or via computational techniques, mainly focusing on the nucleation and growth of voids as a result of the matrix–graphite interphase debonding.[15–22] In most papers, the fracture surface analysis has been a brief secondary study. Therefore, it is very difficult to extract information from a fractographic analysis after a fracture occurs, and consequently, one of the most relevant diagnostic elements used in the failure analysis is lost. This lack of information may become a limiting factor for the application of this material. Recently, the authors presented a study where the fracture surfaces of pearlitic ductile cast iron broken under different loading conditions were exhaustively analysed.[23]

The aim of this investigation is to extend the prior study on the fracture surfaces of pearlitic DI to the analysis of the influence of different test conditions on the fracture surfaces of FDI, focusing on the determination of the predominant fracture mechanisms through the characterisation of the topographic features of the fracture surface. In addition, the study aims at identifying the main crack propagation direction. This research work is intended to provide a better understanding of DI complex fracture processes and to expand the information about the fractographic studies on this material.

EXPERIMENTAL METHODOLOGY

Material characterisation

One inch 'Y' blocks of ductile iron (DI) were cast in sand moulds (ASTM A897M). The chemical composition was determined with a Baird DV6 spectrometer. All 'Y' blocks were ferritised by a heat treatment consisting of an austenitising stage at 920 °C for 4 h followed by a slow cooling down to room temperature. Metallographic samples were prepared by means of standard polishing and etching methods. Etching was carried out employing nital (2%). The microconstituents as well as the nodule count, nodularity and nodule size were quantified by using an optical microscope OLYMPUS PMG3 and the Image-Pro Plus software.

Mechanical testing

Brinell hardness measurements were performed with a universal hardness testing machine 'Ibertest', Model 'DU-250' following the recommendations of ASTM E10-01. V-notched Charpy impact specimens of $10 \times 10 \times 55$ mm for impact and three-point bending test (ASTM E23) and single-edge notched bending (SEN (B)) specimens of $10 \times 20 \times 90$ mm for fatigue test (ASTM E399) were machined from Y blocks. All reported values of mechanical properties are the average of at least three tests. Impact testing was carried out at four different temperatures by using a pendulum AMSLER 130/688, with maximum energy of 300 J. Three-point bending tests under quasi-static loading were performed through a universal testing machine Morh & Federhaff with a crosshead displacement rate of 8.4×10^{-3} mm s^{-1}. For the fatigue test, SEN(B) specimens were used. A high-cycle fatigue regime was performed in a displacement-controlled mechanical testing machine with a double eccentric actuator. A constant eccentricity of $e = 0.145$ mm, which induces a maximum load of 2 kN, was applied.[24] A stress ratio $R = 0$ was chosen for all tests. Stable crack propagation was attained following these conditions under small-scale plasticity. The frequency of the cyclic load was of 25 Hz. Table 1 shows the specimen's identifications for the different testing conditions

RESULTS AND DISCUSSION

Chemical composition and microstructures

The chemical composition of the melt is listed in Table 2. The as-cast microstructure characterisation according to the ASTM A 247 standard and the Brinell hardness are listed in Tables 3 and 4 respectively. The nodularity was

Table 1 Summary of label used for each test conditions

Sample label	Matrix	Test	Test temperature (°C)
FI-20	Ferritic	Impact	−20
F10			0
F120			20
F160			60
Fflx.		Bending	20
Ffat.		Fatigue	20

Table 2 Chemical composition of DI used in the present study (wt%)

C	Si	Mn	S	P	Mg	Cu	Ni	Cr
3.32	2.36	0.31	0.012	0.016	0.033	0.62	0.025	0.058

Table 3 Metallographic as-cast characterisation

Nodule count (nodules mm^{-2})	Nodularity	Nodule size
100	>95%	6

Table 4 Hardness value of as-cast and ferritised samples

Matrix	Label	Brinell hardness
Ferritic	C1F	149
As-cast (pearlitic)	AC	272

considered suitable for this study. The microstructures as-cast and after ferritising are shown in Fig. 1. As-cast microstructure shows a fully pearlitic matrix. After the ferritising heat treatment, the microstructure results in fully ferritic structure.

Analysis of fracture surfaces by SEM

Figure 2 shows the fracture surfaces generated under impact loading at different temperatures. All surfaces showed graphite nodules and empty cavities left by graphite nodules that were detached from the matrix during the fracture process. At low temperatures (−20 °C, Fig. 2a), the surface shows cleavage facets with river patterns. The graphite nodule cavities show very little strain. Both observations support a predominantly brittle failure mode. As the temperature increases to 0 °C (Fig. 2b), cleavage facets continue to dominate, but the nodular cavities show greater straining. At room temperature (Fig. 2c), a significant fraction of the surface shows ductile dimples, while the remaining surface shows cleavage facets. In addition, the nodule cavities show extensive deformation. As the test temperature rises to 60 °C, Fig. 2d, cleavage facets are no longer present, but the fracture surface is dominated by dimples formed after microvoid coalescence.

The examination at higher magnification, Fig. 3a, shows that, even for the test carried out at −20 °C, the matrix portions surrounding non-metallic inclusions show some degree of plastic deformation, demonstrating that some microplasticity is associated with the fracture mechanism. On the other hand, Fig. 3b shows detailed features of the cleavage facets, where river patterns of different size are noticed.

Figure 4 shows the fracture surface of samples broken under impact loads tested at different temperatures. It must be noticed that the energy involved in the fracture increases about three times (from 72 to 200 kJ m^{-2}) as the temperature changes from −20 to 60 °C. Nevertheless, only small changes in the extent of macroscopic plastic deformation can be noticed as the temperature increases. On the other hand, the brightness of the surfaces changes markedly, reflecting the drastic changes in the microscopic fracture mechanism detailed previously in the text.

Figure 5shows the fracture surface resulting from the three-point bending test at room temperature under quasi-static loading. A fully ductile fracture micromechanism dominates the surface, as dimples and highly deformed graphite nodule cavities are found. No cleavage fracture facets are seen. Noticeable differences in the predominant fracture mode are found as the fracture surfaces generated at room temperature (20 °C) by impact and quasi/static bending loading are compared. After the three-point bending test, the fracture surface shows a very rough topography and a much higher surface area occupied by graphite when compared with the fracture surface resulting from the impact testing, where some disperse cleavage facets can be found, as shown in Fig. 6. This apparently higher nodular density is not real, as all samples have identical nodular count, but it is caused both by the greater enlargement of the nodular cavities as a result of the plastic deformation that takes place when the loading is slow and by the tortuosity of the crack path that led to higher roughness, exposing a higher number of graphite nodules on the fracture surface.

The fracture surface found after 1.8×10^5 fatigue cycles is shown in Fig. 7. At low magnification, the

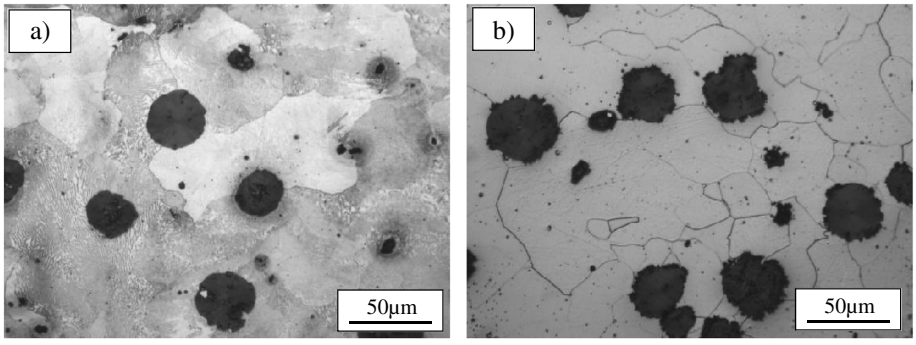

Fig. 1 Optical micrographs. (a) As-cast (pearlitic) and (b) after the annealing heat treatment (ferritic).

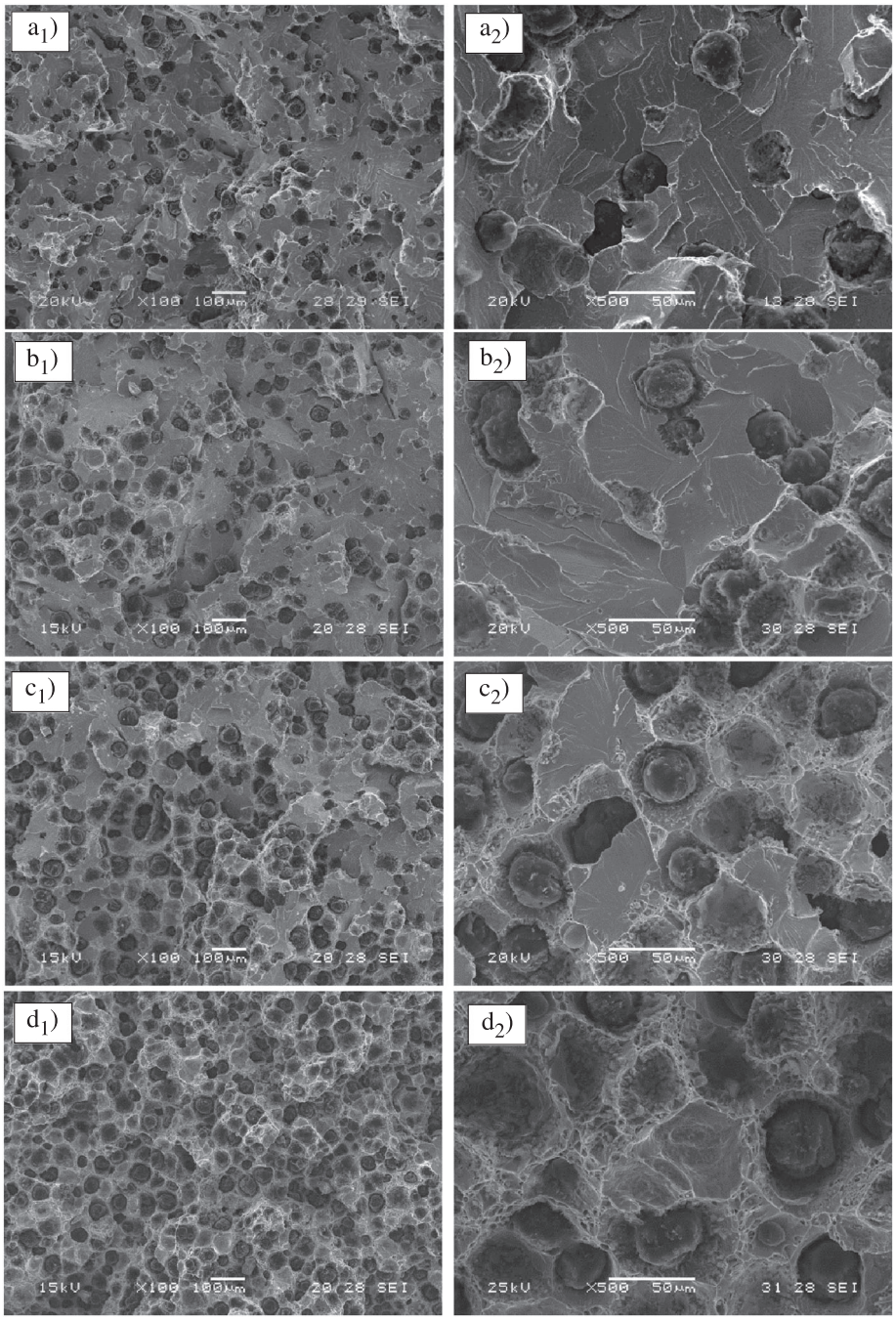

Fig. 2 Fracture surfaces generated under the impact test at different temperatures. (a) −20, (b) 0, (c) 20 and (d) 60 °C.

surface is irregular, and its basic features cannot be observed. As the magnification is increased, the surface shows flat facets that appear to be cleavage facets. Nevertheless, these facets are different from the cleavage facets shown on impact samples at low temperature (Fig. 3). Little or no indication of ductile fracture mechanisms is found. The graphite nodule cavities show very little deformation. A number of small secondary cracks are found on the fracture surface, many located at the vicinity of the graphite nodules. Some examples are pointed by arrows in Fig. 7b. The fatigue crack path can be investigated by optical metallography on a transverse section of a fatigue sample in which the test has stopped before break (Fig. 8). The crack path shows frequent changes in direction, apparently in an attempt to include graphite nodules and favourably oriented ferrite grain boundaries. A number of secondary cracks can be also observed (white arrow).

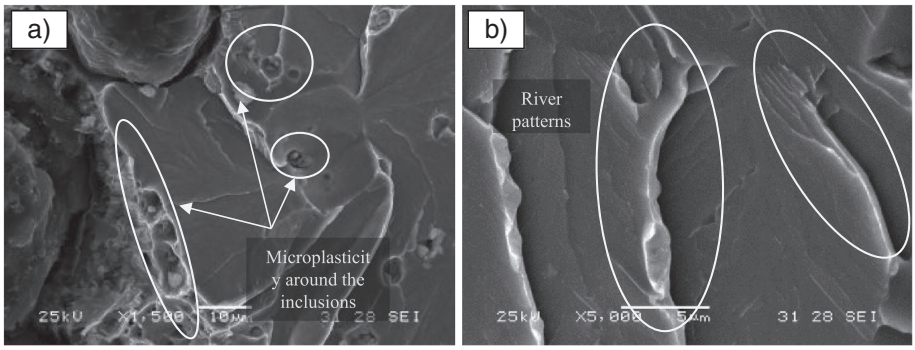

Fig. 3 Fracture surfaces of ferritic ductile iron tested at −20 °C.

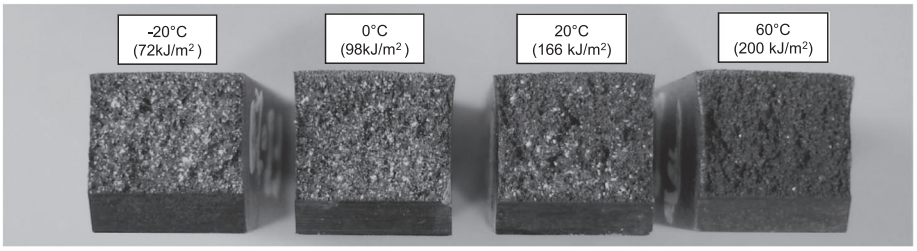

Fig. 4 Macroscopic fracture surface of the specimens broken under impact loads.

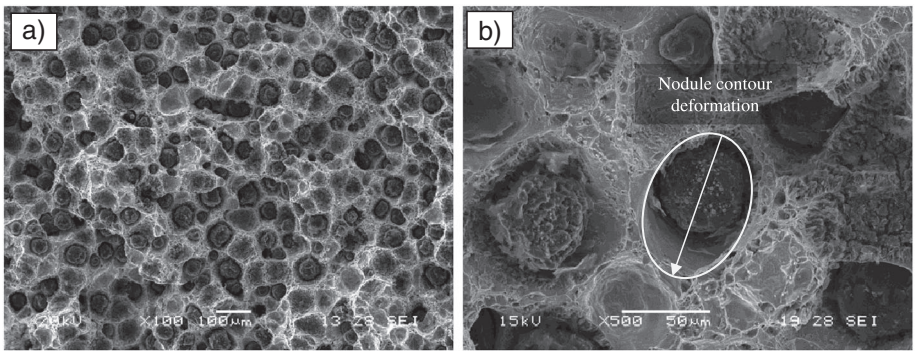

Fig. 5 Fracture surfaces of the specimens broken under quasi-static loads.

The typical fatigue striations are not easily found on the fracture surface. A careful examination at higher magnification allows the observation of relatively small areas in which fatigue striations are clearly recognised, as shown in Fig. 9.

Direction of macroscopic propagation and its relation with the topographic features

With the goal of identifying the direction of propagation of fracture, the topographic features of the fracture surfaces were analysed carefully for the different loading conditions investigated. The samples were observed at the centre of the fracture surface so that the edge effects are negligible, as shown in Fig. 10.

Brittle failure mode

As mentioned in the section on Analysis of fracture surfaces by SEM, brittle fracture mechanisms with cleavage facets showing the classical river patterns were observed in the samples broken under impact loading at lower temperature. The literature reports that different cleavage facets converge and join into a single crack, forming the river patterns, and that the direction of the river pattern is consistent with the local crack propagation direction.[3] Therefore, considering that the mechanical tests impose a known direction of propagation of the main crack, the SEM fractographies can be made keeping track of such direction. Then, it becomes possible to compare the local crack propagation direction along a cleavage facet with

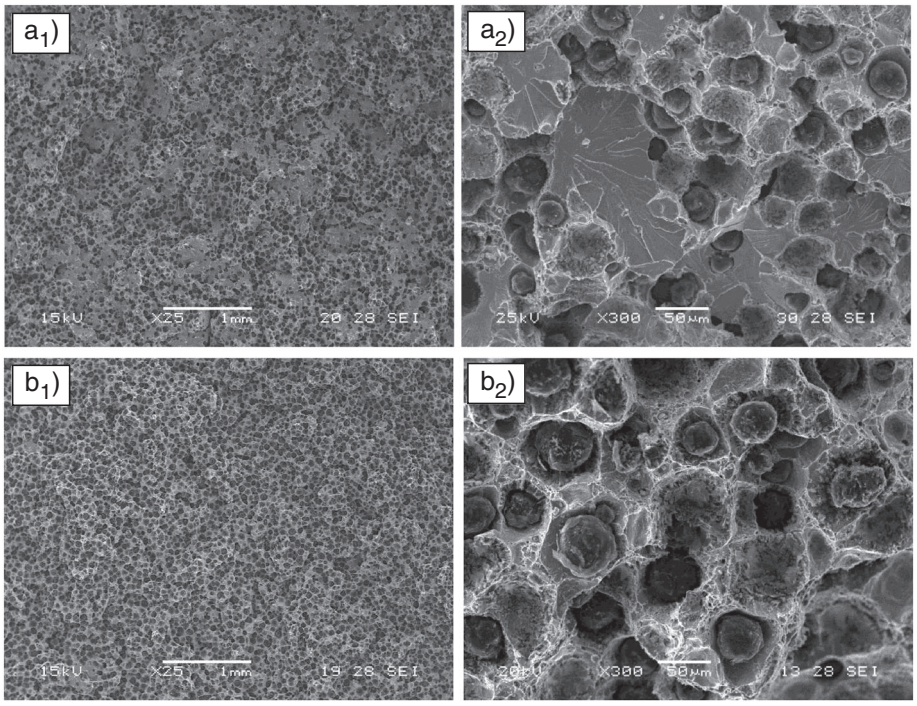

Fig. 6 Fracture surfaces of the specimens broken at room temperature (20 °C) under (a) impact loads and (b) quasi-static loads.

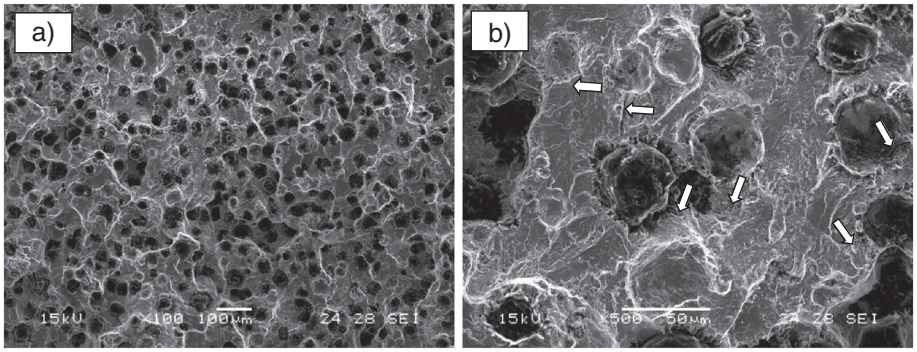

Fig. 7 Fracture surfaces of the specimens broken under the high-cycle fatigue regime. Different magnifications.

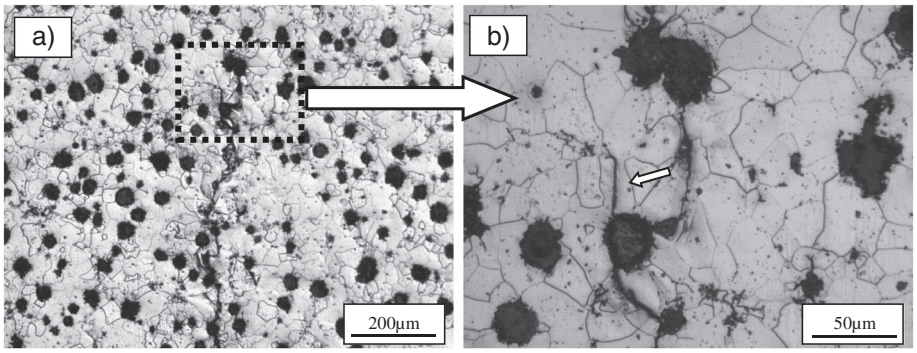

Fig. 8 Optical metallography showing the fatigue crack path.

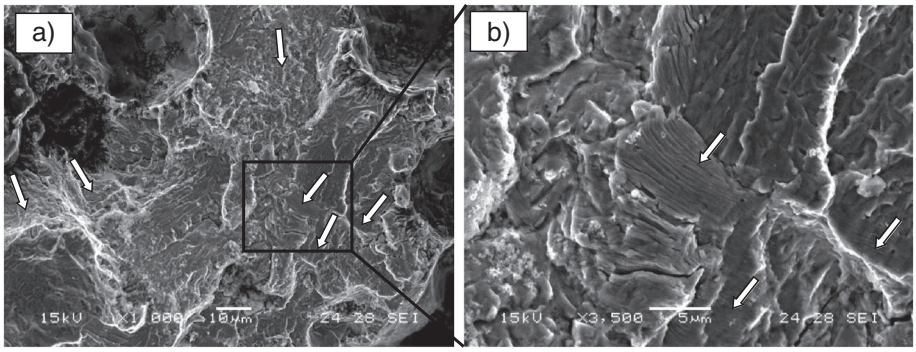

Fig. 9 Fracture surfaces of the specimens broken under the high-cycle fatigue regime. Small regions showing striation marks.

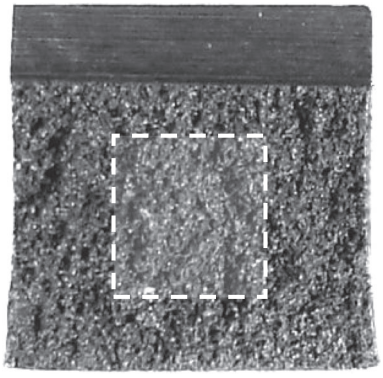

Fig. 10 Sample area used for the analysis of the direction of macroscopic crack propagation.

the main crack propagation direction. The experimental methodology used was described in an earlier investigation of the fracture of pearlitic DI as methodology 1, where local propagation vectors (each one identified at the point in which two river patterns join) were characterised by the angle formed with respect to the main crack propagation direction.[23] One of the SEM fractographies analysed is shown in Fig. 11a. For a better interpretation of the dataset, histograms of the relative frequencies of local angles are plotted, as shown in Fig. 11b. The local directions were grouped into 20 intervals ranging from −180° to 180°. The reference angle, this is the direction of the main crack propagation, is set to 0°. The result of the characteristic statistical dataset (mean, median and mode) and the counts made are listed in Table 5. In all cases, the mean (M) and the median (Me) of the dataset were between −10° to 10°, and the mode value (Mo) of the distribution was 0°. These results not only show that the average of local directions tends to coincide with the macroscopic propagation direction but also show that the highest relative frequency of local angles is observed in this direction. These conclusions are in coincidence with the results of an earlier investigation on pearlitic DIs.[3]

Ductile failure mode

When the specimens are broken under impact loads at higher temperatures, or under slow bending, only small

Table 5 Statistical dataset obtained from the joint of each cleavage facet

	FI-20
Mean	9 ± 2
Median	9
Mode	0
Counts	1515

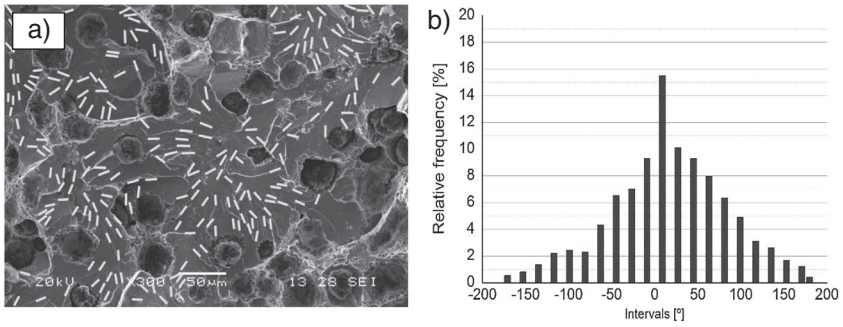

Fig. 11 Quantitative analysis on SEM fractographies by means of the Image-Pro Plus software. (a) Fractography quantified and (b) histograms from dataset.

and disperse cleavage facets can be observed on the fracture surface, as shown in Fig. 3d. This relatively small proportion of cleavage patterns did not allow obtaining a good assessment of the crack propagation direction by the analysis of the river patterns. Instead, a different method was developed to determine the propagation direction when the ductile fracture is the predominant failure mode. The hypothesis is that the predominant fracture mechanism is promoted by an initial stage of matrix–graphite nodule decohesion and the subsequent enlargement of the cavities formed by plastic deformation. As the loading increases, the cavities enlarge until necking takes place at the bridges between adjacent holes. It is assumed that the plastic deformation will be influenced by the loading conditions and the crack propagation direction. Therefore, a method to identify the crack propagation direction based on the measurement of the plastic deformation of the metallic matrix surrounding the graphite nodules is proposed. The characterisation of the morphology of the cavities is carried out on digital images of the fracture surface observed under a graphic environment. For each nodule present at the fracture surface, an ellipse is manually defined with the best possible fit to the deformed nodular contour. Then, two different measurements were carried out. First, the length of the nodular contour in parallel (Y) and perpendicular (X) axes to the main crack propagation direction was measured, as shown in Fig. 12. In addition, the angle formed between the major axis of the ellipse and the main crack propagation direction was measured. The methodology demands time and care. The results of the measurements of the ratio Y/X and the angle (α) on several fields of the two samples investigated are listed in Table 6. The results are grouped depending on the value of the Y/X ratio. The larger proportion of the nodular cavities show values of Y/X greater than one, that is, the nodular cavities tended to strain according to the main crack propagation.

For a better interpretation of the dataset, a histogram and a function of cumulative frequency of the X/Y ratio are plotted in Fig. 13. The results show that in the impact sample, 66% of the total readings had a ratio $Y/X > 1$, while in the bending case, this value increased to 77%. The values of α show mean values of $2.7° \pm 0.2°$ and $0.8° \pm 0.2°$ for the bending and the impact at 60 °C samples respectively.

Taking into account that the reference axis has been set in the main crack propagation direction, it can be concluded that this method allows identifying the main crack propagation direction with good approximation. It must be noted that the result will be independent from the reference axis chosen, as will be the case when a fracture surface of unknown crack propagation direction is examined. However, even though the method has been able to identify the main crack propagation direction under the current experimental conditions, the effectiveness of the methodology proposed has to be evaluated under other testing conditions and specimen geometry before it can be regarded as a general method.

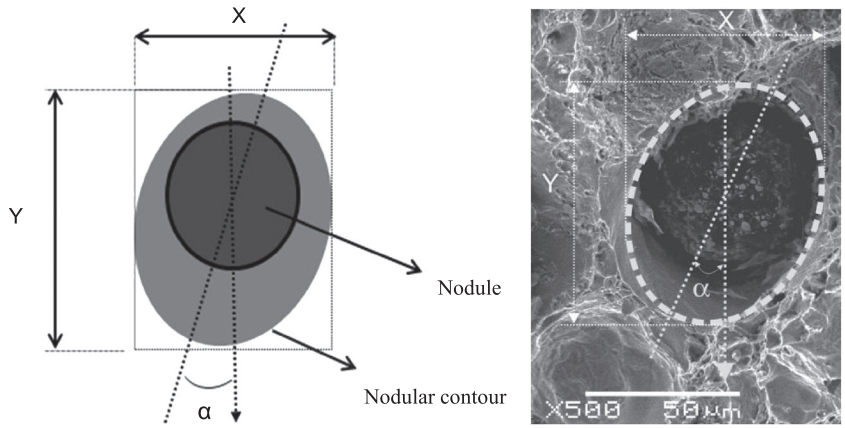

Fig. 12 Method used to measure the parameters that characterise the nodule contour deformation. Ductile fracture.

Table 6 Deformation of the nodular contour on the fracture surface

Sample	Y-axis predominant (%)	Equiaxial (%)	X-axis predominant (%)	Contours analysed	Angle of equivalent ellipse (α)
FI60	66	23	10	254	$2.7 \pm 0.2°$
Fflx	77	15	8	135	$0.8 \pm 0.2°$

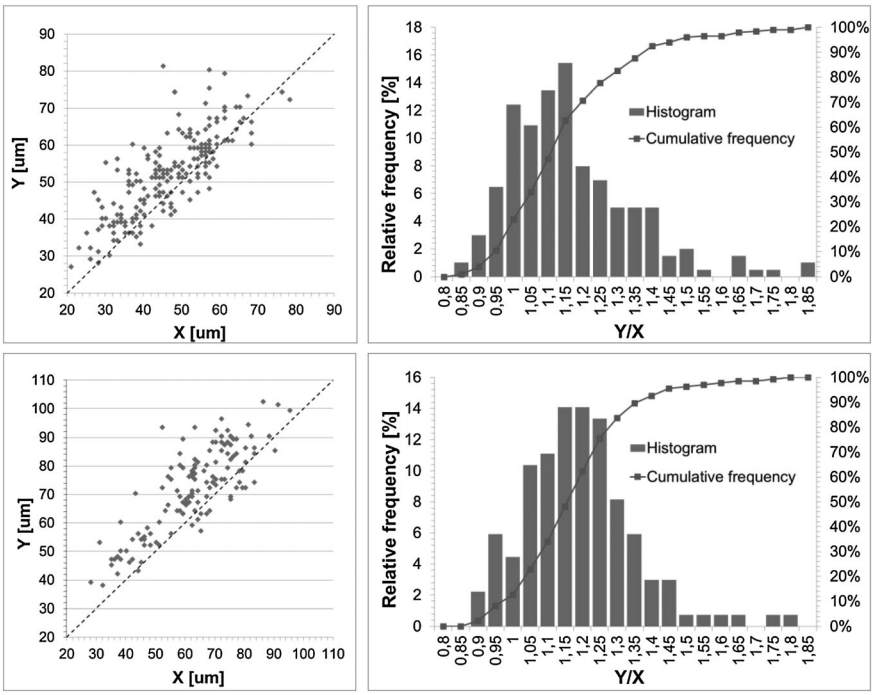

Fig. 13 Statistic plots from the experimental measurements of the *X/Y* ratio. (a) FI60 and (b) Fflx.

Fatigue

As pointed out in the section on Analysis of fracture surfaces by SEM,, the fracture surfaces typically found after fatigue testing show flat facets that appear to be cleavage facets at low magnification and little or no indication of ductile fracture mechanisms. A careful examination at higher magnification showed relatively small areas in which fatigue striations are clearly recognised. Several measurements of the striations were carried out as shown in Fig. 14. The mean value of the distance between striation marks was 0.46 ± 0.03 μm.

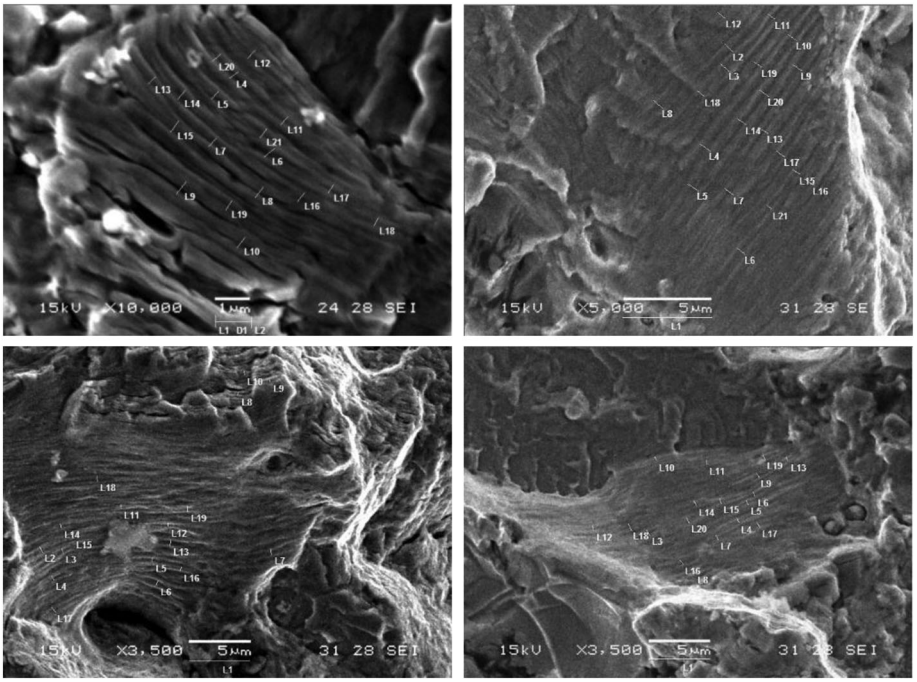

Fig. 14 Fracture surface of the samples broken under cyclic loading condition. Detail of the measurements of the striations.

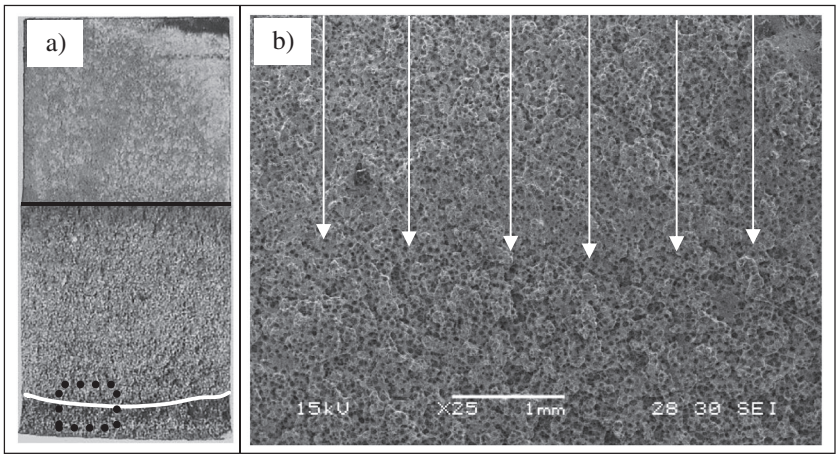

Fig. 15 Fracture surface of the samples broken under cyclic loading condition. (a) Macroscopic photography and (b) SEM fractography of the area of the black dotted zone.

An attempt was made to compare the average direction of crack propagation of the striated portions of fracture. Unfortunately, no clear correlation between the main crack propagation direction and the average crack propagation direction of the striated portions was found. It is apparent that, under the loading conditions investigated and at the microscopic level, multiple fatigue cracks progress simultaneously following different directions. Therefore, the proportion of striated fracture facets is scarce, and their orientations diverse. These results suggest that the direction of propagation of macroscopic fatigue cracks cannot be identified by means of the analysis of the fracture surface at the microscopic level under the test condition used. On the other hand, some indications of the macroscopic propagation of the crack are evident on the fracture surface, as shown in Fig. 15. In Fig. 15a, the border between the notch and the stable zone is marked by a solid black line, while the border between the stable propagation of the fatigue crack and the final collapse (that can be easily noticed although the difference in the surface topography is not as marked as in the case of steel) is marked by a solid white line. Some oxide marks that were produced during the specimen manipulation after the test can be also seen. In Fig. 15b, the SEM image of the square black dotted zone observed in the macroscopic photography is shown

CONCLUSIONS

The fracture surfaces of FDI broken under impact, bending and fatigue loading conditions were characterised and compared by analysing SEM microscopy images.

- The results show that the predominant failure mode suffers notorious changes as a function of the loading conditions and test temperatures that lead to fracture of FDIs.
- Two different methods to identify the direction of the macroscopic crack propagation have been proposed, one applicable to brittle fracture and the other to ductile fracture. The methods require considerable time and effort but can calculate the direction of propagation of the macroscopic crack with good accuracy under the experimental conditions examined. These methods can provide relevant additional information to the fractographic analysis.
- The examination of the fatigue fracture surfaces of FDI showed very little portions presenting striation marks. No method was found to identify the direction of propagation of the main crack in the case of fatigue cracks.

REFERENCES

1 Burditt, F. M. (1992) *Ductile Iron Handbook*. American Foundrymen's Society, Inc., Des Plaines, Illinois, USA, pp. 31–36.
2 Davis, R. J. (1990) *Metals Handbook*, Vol. **11**, 9th edn, Failure Analysis and Prevention. American Society for Metals, Ohio, USA.
3 Fellows, A. J. (1973) *Metals Handbook*, Vol. **9**, 8th edn, Fractography and Atlas of Fractographs. American Society for Metals, Ohio, USA.
4 Anderson, T. L. (1995) *Fracture Mechanics: Fundamentals and Applications*, 2nd edn, CRC Press, Boca Raton, Florida, USA. pp. 265–305.
5 Barsom, J. M. and Rolfe, S. T. (1987) *Fracture and Fatigue Control in Structures, Application of Fracture Mechanics*, 2nd edn, Englewood Cliffs, New Jersey 07632 USA.
6 Broek, D. (1991) *Elementary Engineering Fracture Mechanics*, 4th edn, 101 Philip Dr., Kluwer Academic Publishers, Norwell, MA 02061 USA.

7 Nobuki, T., Hatate, M. and Shiota, T. (2011) Notch Effects on Impact and Bending Characteristics of Spheroidal Graphite and Compacted Vermicular Graphite Cast Iron with Various Matrices. *Key Eng. Mat.*, **457**, 392–397.
8 Akdemir, A., Tekeli, M. and Ataberk, N. (2007) Fatigue crack growth behavior in ferritic ductile iron with surface crack under reverse bending. *Comp. Mater. Sci.*, **41**, 38–43.
9 Di Cocco, V., Iacoviello, F. and Cavallini, M. (2010) Damaging micromechanisms characterization of a ferritic ductile cast iron. *Eng. Fract. Mech.*, **77**, 2016–2023.
10 Bonora, N. and Ruggiero, A. (2005) Micromechanical modeling of ductile cast iron incorporating damage. Part I: Ferritic ductile cast iron. *Int. J. Solids Struct.*, **42**, 1401–1424.
11 Cavallini, M., Di Bartolomeo, O. and Iacoviello, F. (2008) Fatigue crack propagation damaging micromechanisms in ductile cast irons. *Eng. Fract. Mech.*, **75**, 694–704.
12 Hafiz, M. F., Hammouda, A. and El-Gemae, S. (2005) Impact properties and fractography of spheroidal graphite cast irons. *AFS Trans., Schaumburg, II, USA*, **5**, 2–12.
13 Pokluda, J. and Siegel, J.(1990) Mixed fatigue fracture morphology of ferritic ductile iron. *Fatigue Fract. Eng. Mater. Struct.*, **13**, 375–385.
14 Martinez, R. (2010) Fracture surfaces and the associated failure mechanisms in ductile iron with different matrices and load bearing. *Eng. Fract. Mech.*, **77**, 2749–2762.
15 Toktaş G., Tayanç M. and Toktaş A. (2006) Effect of matrix structure on the impact properties of an alloyed ductile iron. *Mater Charact*, **57**, 290–299.
16 Dong, M. J., Prioul, C. and François, D. (1997) Damage effect on the fracture toughness of nodular cast iron: part I. Damage characterization and plastic flow stress modeling. *Metall. Mater. Trans. A*, **28**, 2245–2254.
17 Guillermer-Neel, C., Feaugas, X. and Clavel, M. (2000) Mechanical behavior and damage kinetics in nodular cast iron: part I. Damage mechanisms. *Metall. Mater. Trans. A*, **31**, 3063–3074.
18 Liu, J. H., Hao, X. Y., Li, G. L. and Liu, G. Sh. (2002) Microvoid evaluation of ferrite ductile iron under strain. *Mater. Lett.*, **56**, 748–55.
19 Voigt, R. C., Eldoky, L. M. and Chiou, H. S. (1986) Fracture of ductile cast irons with dual matrix structure. *AFS Trans.*, **94**, 645–656.
20 Eldoky, L. and Voigt, R. C. (1986) Crack initiation and propagation in quenched and tempered ductile cast iron. *AFS Trans.*, **86**, 631–636.
21 Berdin, C., Dong, M. J. and Prioul, C. (2001) Local approach of damage and fracture toughness for nodular cast iron. *Eng. Fract. Mech.*, **68**, 1107–1117.
22 Zhang, K. S., Bai, J. B. and François, D. (1999) Ductile fracture of materials with high void volume fraction. *Int. J. Solids Struct.*, **36**, 3407–3415.
23 Fernandino, D.O. and Boeri, R. (2014) Fracture of pearlitic ductile cast iron under different loading conditions. *Fatigue and Fracture of Engineering Materials and Structure*, **00**, 1–11. DOI: 10.1111/ffe.12220.
24 Tada, H., Paris, P. C. and Irwin, G. (2000) *The Stress Analysis of Cracks Handbook*, 3rd ed. ASME press, New York. Part II, pp 58–59.